

Domain Wall Fermion Study of Scaling in Non-perturbative Renormalization of Quark Bilinears and B_K

Y. Zhestkov

Physics Department, Columbia University, New York, NY 10027

(February 8, 2001)

Abstract

We compute non-perturbatively the renormalization coefficients of scalar and pseudoscalar operators, local vector and axial currents, conserved vector and axial currents, and $O_{LL}^{\Delta S=2}$ over a wide range of energy scales using a scaling technique that connects the results of simulations at different values of coupling β . We use the domain wall fermion formulation in the quenched approximation at a series of three values of β , 6.0, 6.45, and 7.05, corresponding to lattice spacing scaling by factors of two.

I. INTRODUCTION

Lattice QCD has proven to be a powerful approach to calculating from the first principles the mass spectrum, weak decay constants, weak matrix elements, quark masses, and hadronic structure functions. Such studies require calculating matrix elements of composite operators. In order to extract physical predictions in the continuum limit from Monte-Carlo simulations in lattice QCD, one in general needs to determine the normalization of these operators in terms of physical requirements.

In calculations involving the operator product expansion one needs to know the Wilson coefficients. The corresponding calculations are done perturbatively, and therefore must be carried out at a high enough energy scale. To evolve those coefficients down to the scale at which lattice calculations are performed, one usually also uses perturbative methods.

A possible approach to renormalization of operators defined on the lattice is lattice perturbation theory. This approach, though, suffers from many difficulties, the main being poor convergence of the perturbation series. One source of this difficulty was identified by Parisi and Toe [1], and later by Lepage and Mackenzie [2], and is due to the presence of tadpole diagrams. The authors of [2] proposed a method to improve the convergence properties of these series which is known as tadpole-improved perturbation theory. Nevertheless, the calculations using this method are complex, and therefore are rarely carried out beyond the one-loop level. Since g^2 decreases only logarithmically with decreasing a , the systematic improvement of perturbation theory is very difficult, leaving the possibility for large systematic uncertainty in extraction of physical results.

In some limited cases renormalization of lattice operators can be obtained from Monte-Carlo simulations using the chiral Ward Identities. The examples include vector and axial vector currents, and the ratio of pseudoscalar and scalar densities. Unfortunately, this method cannot be applied to general composite operators for which there is no corresponding Ward Identity.

A method for full non-perturbative renormalization of lattice operators by means of Monte-Carlo simulations was proposed in [3]. The procedure mimics the approach taken in continuum perturbation theory. The renormalization conditions are imposed directly on quark and gluon Green's functions, in a fixed gauge, with specified, external lines carrying far off-shell momenta. This defines the so-called Regularization Independent scheme (RI). At high momenta the results can be directly related to the perturbative calculations, provided that corresponding conversions are made in order to match different renormalization schemes used in continuum calculations (usually the \overline{MS} scheme).

A necessary condition for the RI method to work is to have the off-shell momentum scale of the external lines, μ , much smaller than the inverse lattice spacing and much larger than Λ_{QCD} . The former condition restricts the value of reliable momenta from above for a given lattice spacing a . The lower bound on momentum comes from the need to compare with perturbation theory which is only applicable at an energy scale above the non-perturbative regime, $\mu \gg \Lambda_{QCD}$. These two constraints leave a pretty narrow range of momenta that can be used to calculate renormalization coefficients.

To extend the range of momenta over which an operator is renormalized, one can perform simulations at different values of coupling constant $\beta = 6/g^2$ with overlapping regions of reliable physical momenta. By combining the results of these calculations, it is in principle possible to relate renormalization coefficients of a given operator between quite different momentum scales μ . By starting with sufficiently high momenta where the perturbation theory can be trusted, operators can be renormalized at a series of scales down to a few GeV where most lattice calculations are done.

To make the matching between results obtained at different β 's meaningful, it is important to insure that it is done under identical physical conditions. In particular, mass and volume dependence have to be taken into account.

The difficulty that arises from the finite volume effects can be approached in several ways. A direct way of taking the infinite volume limit turns out to be inefficient due to the strong volume dependence at low momenta. In this work we instead keep the volume explicitly finite. The matching between calculations at different β 's is done at the same physical momentum and physical volume. This procedure is described in detail in Section III.

In our simulations we use the domain wall fermion formulation [4]– [7]. This approach is computationally more demanding than the usual Wilson fermions, but offers significant advantages that are more than enough to compensate for the additional computer time required for the calculations. The DWF formulation provides an easy procedure of taking the chiral limit, independently of the continuum limit. No additional fine-tuning is required. By working at sufficiently large lattice extent in the fifth direction, the residual quark mass arising from the chiral symmetry breaking coupling between the walls can be made very small. Then the limit of zero bare quark mass corresponds to the chiral limit with high accuracy. We use this property to eliminate the mass dependence of our results, by taking

the chiral limit.

The excellent chiral properties of the DWF formulation suppresses the mixing of such operators as $O_{LL}^{\Delta S=2}$ with operators of opposite chiralities, Ref. [8]. This is a serious complication for studying the renormalization of such operators using fermion actions with large chiral symmetry violations.

It is important that in the DWF formulation the chiral properties are improved not only for the on-shell calculations, but also for the off-shell ones. This is one of the reasons why the DWF formulation is ideal for using the non-perturbative renormalization method described in the next section that imposes a renormalization condition on the matrix elements of operators between external off-shell quark states. Another important consequence of these good chiral properties of the lattice theory with the DWF is the absence of order $O(a)$ errors in the results for the matrix elements of operators.

We use the quenched version of the DWF method in our paper. For an extensive analysis of the properties of this formulation the reader is referred to the early works on this subject, Refs. [9] and [10].

The paper is organized as follows: In Section II we explain the method of non-perturbative renormalization. The scaling technique is described in Section III. In Section IV we present the results of numerical calculations.

II. THE NON-PERTURBATIVE RENORMALIZATION METHOD

In our calculation of non-perturbative renormalization coefficients we follow closely the procedure first proposed by the Rome-Southampton group [3]. The renormalized operator $O(\mu)$ is defined as the bare operator O_{bare} multiplied by the Z -factor,

$$O(\mu) = Z_O(\mu; a)O_{bare}(a) . \quad (1)$$

For simplicity of presentation we ignore the possibility of operator mixing which would require replacing Eq. (1) by a matrix equation but have no other effect on the method developed in this paper. Here the bare operator $O_{bare}(a)$ is regularized by discretizing it on a space-time lattice with lattice spacing a that has units of inverse energy and throughout this paper a is assumed to be uniform in all directions. It can also depend on other (bare) parameters in the Lagrangian. The renormalized operator $O(\mu)$ has low energy matrix elements with no dependence on regularization parameters. These low energy matrix elements are functions of only physical parameters, such as physical masses, coupling constant, etc., defined at the renormalization scale μ , and μ itself.

The renormalization condition imposed on an operator constructed from a product of n quark fields is given by

$$Z_O(\mu; a)Z_q^{-n/2}(\mu; a)\Gamma_O(p; a)|_{p^2=\mu^2} = 1 , \quad (2)$$

where $Z_q(\mu; a)$ is the quark field renormalization coefficient,

$$q_{ren}(\mu) = Z_q^{1/2}(\mu; a)q_{bare}(a) . \quad (3)$$

This specifies our conventions for Z_q . The precise prescription for determining Z_q is given later in Eq. (6).

The quantity $\Gamma_O(p)$ is obtained from the amputated matrix element of the operator O_{bare} between external off-shell (bare) quark states, in the Landau gauge, by tracing it with a projector \hat{P}_O on a tree-level operator. In the case of quark bilinear operators it is defined by the equation

$$\Gamma_O(p; a) = \frac{\text{Tr} \left(\Lambda_O(p; a) \hat{P}_O \right)}{12}, \quad (4)$$

where

$$\Lambda_O(p; a) = S_{bare}(p; a)^{-1} G_O(p; a) S_{bare}(p; a)^{-1} \quad (5)$$

is the truncated Green's function. The corresponding equations for the case of four quark operators can be found in Section IV D of this paper.

The above renormalization condition is independent of the regularization scheme, although it does depend on a particular choice of the off-shell momenta and the choice of gauge. This dependence is not important since the final physical results will not depend on this momentum choice, and will be gauge invariant. We always choose the sum of all external momenta to be equal to zero. In the case of the four quark operators all four external lines carry momenta that are equal up to an overall sign.

The renormalization coefficient of the fermion field, $Z_q^{1/2}$, is defined from the full propagator,

$$Z_q(\mu; a) = -\frac{i}{48} \text{Tr} \left(\gamma^\mu \frac{\partial S_{bare}(p; a)^{-1}}{\partial p_\mu} \right)_{p^2=\mu^2} \quad (6)$$

and can be calculated numerically using the Ward Identity for the conserved vector current V^C in the form

$$\Lambda_{V^C}^\mu(p; a) = -i \frac{\partial S_{bare}(p; a)^{-1}}{\partial p_\mu}, \quad (7)$$

which implies

$$Z_q(\mu; a) = \frac{1}{48} \text{Tr} \left(\gamma^\mu \Lambda_{V^C}^\mu(p; a) \right)_{p^2=\mu^2}. \quad (8)$$

Substituting this into Eq. (2) for V^C one can see that the RI renormalization condition for the conserved vector current is consistent with the equality $Z_{V^C} = 1$.

III. SCALING TECHNIQUE

Our scaling technique exploits the renormalizability of lattice QCD which implies that, when scaling violations are small, the values of a renormalization coefficient calculated at two different values of the lattice spacing will be related to each other by an overall multiplicative coefficient independent of the physical conditions such as physical volume or momentum scale,

$$\frac{Z_O(\mu, V; a')}{Z_O(\mu, V; a)} = R_O(a', a) \quad (9)$$

We use this property to “sew together” evolutions of renormalization coefficients over overlapping regions of momentum scale. We are going to describe this technique in detail here.

In the formula above we explicitly show the dependence of the renormalization coefficients on the physical volume V . While this dependence could be eliminated by taking the infinite volume limit, in our scaling method this is not necessary for the intermediate steps where the finite volume effects are explicitly taken into account. To avoid complications associated with the quark mass renormalization, the chiral limit is always taken.

In any Monte–Carlo QCD simulation the size of the lattice in any direction is finite and rarely exceeds 32. This puts limits on the momenta accessible in a simulation with one fixed value of the coupling constant β . The components of momenta can assume only a discrete set of values,

$$p_i a = \frac{2\pi}{L_i} n_i, \quad n_i = -(L_i - 1)/2, \dots, 0, \dots, L_i/2. \quad (10)$$

For the momenta with large values of n_i the discretization errors become significant. This forces one to use momenta with small n_i and therefore limits the range over which the non–perturbative renormalization technique outlined above can be carried out.

Finding a way to study the renormalization of operators in a wide range of momentum scales is important in many applications. One particular but very important example is the connection with perturbation theory. Most of the lattice simulations are performed at low momentum scales, where the non–perturbative effects play a major role. On the other hand, if one needs to relate the results to perturbation theory, for example, to use the Wilson coefficients determined from a perturbative calculation, one has to have access to large physical momenta (several GeV) where perturbation theory should become accurate. This is very difficult to achieve in a simulation at a single value of β .

It is natural to think of using the results of numerical simulations at several β ’s with overlapping regions of physical momenta with small discretization errors to extend the range over which renormalization coefficients are calculated numerically. The procedure implementing this idea is the following (see Figure 1). One starts at $\beta(a)$ which is sufficiently large to insure that there are momenta well below the lattice cutoff that are in the perturbative regime. At such scales the renormalization coefficients obtained from the Monte–Carlo simulation can be reliably related to the perturbative ones. The finite volume effects at this $\beta(a)$ can be eliminated by numerically taking the infinite volume limit. Alternatively, one can use perturbation theory carried out at finite volume.

The next step involves simulations at a series of β ’s with lattice spacing a increasing by factors of two. The number of lattice sites in all directions is fixed. The physical volume is finite and different in each simulation, increasing by factors of 2^4 . The range of momenta with small discretization errors in each simulation also scales by factors of two. The overall range of momentum scales with small discretization errors covered in this sequence of simulations can be very large. But the Z –factors obtained with different lattice spacings cannot be meaningfully compared directly, since the lattice spacing plays the role of the ultraviolet cutoff on the lattice. Changing the cutoff requires complex,

generally nonperturbative renormalization of operators in order to keep the physical, low energy predictions of the theory unchanged. Therefore, in order to relate the Z -factors obtained in simulations at different β 's, it is necessary to rescale them to be defined with the same ultraviolet cutoff equal to the lattice spacing a at some fixed value of β . To achieve this, we use the property Eq. (9) which lies in the heart of our scaling method. For the common ultraviolet cutoff we choose, quite arbitrarily, the lattice spacing at $\beta = 7.05$ from the first simulation in the series.

In order to accomplish the program of redefining all of the Z -factors at a common ultraviolet cutoff a it is necessary to know the coefficients $R_O(a, a')$ that relate the Z -factors computed at the cutoff a' to the Z -factors that would be found if the cutoff a was used instead. To compute the rescaling coefficients $R_O(a, a')$ we perform a series of additional simulations. Each additional simulation has the lattice spacing two times larger than the corresponding simulation from the main series. At the same time, the number of the lattice sites in each direction is reduced by a factor of two. With this choice of parameters, the physical volume and the values of physical momenta are the same for these two simulations. If discretization errors were negligible, the Z -factors from these two simulations computed at the same physical momenta would be related by a momentum-independent factor $R_O(2^n a, 2^{n+1} a)$, in accordance with Eq. (9). Here $2^n a$ and $2^{n+1} a$ are the lattice spacings used correspondingly in the simulation from the main series and the additional simulation, while a is the value of the common ultraviolet cutoff chosen to be equal to the lattice spacing used in the simulation with the largest β in the series. To find this factor we would use the ratio $Z(\mu, V; 2^n a)/Z(\mu, V; 2^{n+1} a)$ calculated at any value of physical momentum scale μ . Here V is the physical volume in both simulations.

When discretization errors are present, Z -factors, as well as their ratios, have momentum-dependent corrections. For the domain wall fermion action these errors are quadratic in momentum,

$$\frac{Z_O(\mu, V; 2^n a)}{Z_O(\mu, V; 2^{n+1} a)} = R_O(2^n a, 2^{n+1} a) + O((\mu 2^n a)^2) . \quad (11)$$

We use quadratic in μa fits to remove the $O((\mu 2^n a)^2)$ term and extract $R_O(2^n a, 2^{n+1} a)$. By combining the rescaling coefficients obtained for pairs of lattice spacings, $R_O(a, 2a)$, $R_O(2a, 4a)$, etc., we can compute the rescaling coefficients $R_O(a, 2^n a)$,

$$\begin{aligned} R_O(a, 2a) \\ R_O(a, 4a) &= R_O(a, 2a)R_O(2a, 4a) \\ R_O(a, 8a) &= R_O(a, 2a)R_O(2a, 4a)R_O(4a, 8a) \\ &\dots, \end{aligned} \quad (12)$$

or, more generally, $R_O(2^n a, 2^m a)$ where n and m are integers.

With the rescaling coefficients on the left hand side of equations Eq. (12) we finally can apply the same formula Eq. (9) to the Z -factors computed in the main series of simulations at different ultraviolet cutoffs to compensate for the non-trivial renormalization required when different values of the cutoff are used. In particular, from the original Z -factors in the main series, $Z_O(\mu, V; a)$, $Z_O(\mu, 2^4 V; 2a)$, $Z_O(\mu, 4^4 V; 4a)$, etc., we obtain $Z_O(\mu, V; a)$, $Z_O(\mu, 2^4 V; a)$, $Z_O(\mu, 4^4 V; a)$, etc.,

$$\begin{aligned}
& Z_O(\mu, V; a) \\
Z_O(\mu, 2^4V; a) &= R_O(a, 2a)Z_O(\mu, 2^4V; 2a) \\
Z_O(\mu, 4^4V; a) &= R_O(a, 4a)Z_O(\mu, 2^4V; 4a) \\
& \dots
\end{aligned}
\tag{13}$$

After such a rescaling the ratios of the new Z -factors from all of the simulations are completely physical and represent the dependence of the corresponding quantities on the momentum scale and volume. We would like to emphasize that direct computation of the Z -factors on the left hand side of Eq. (13) in the whole momentum scale range for which they have been determined would require tremendous computer resources and at the very least would be completely impractical.

After the rescaling, the renormalization coefficients Z_O from different simulations evaluated at the same physical momentum scale will in general differ, because they are calculated in different physical volumes. In fact, this method offers one the possibility to study the finite volume effects using same size lattices with nevertheless quite different physical volumes, which can provide certain advantages. The difference caused by the finite volume effects gets smaller when the momentum scale becomes large in comparison with the inverse size of the volume extent. For some renormalization coefficients these effects are quite large (see results for the scalar and pseudoscalar densities and $O_{LL}^{\Delta S=2}$). This effect is illustrated schematically in Figure 1 on the graph at the bottom. The labels on the lines show explicit dependence on the physical volume, which is different for the simulations at different β 's. If the finite volume effects are small, these lines overlap at the corresponding momentum scales. This is (almost) the case for the local and exactly conserved vector and axial currents. For any renormalization coefficient there exists a line that corresponds to the infinite volume. It is shown as a dotted line on the plot at the bottom of Figure 1. Since in our method we do not need to take this limit, our lines are just approximations of the infinite volume line. At each momentum scale the line that has larger physical volume is a closer approximation.

Another reason why the Z -factors computed at the same physical momentum can differ between simulations and in fact from their true values is the presence of discretization errors. We eliminate these errors from the determination of rescaling coefficients R_O using the procedure outlined above, but not from the Z -factors themselves. To remove discretization errors from the Z -factors we could use even more additional simulations with matching physical volumes so that a continuum limit at each momentum could be taken. The presence of these errors does not effect our ability to relate Z -factors between arbitrarily different momenta since we only need R_O for that. Since discretization errors are quadratically small for small lattice momenta, the values of the computed Z -factors at each physical momentum are closer to their true value for data points that come from the simulations at larger β . When the finite volume effects are negligible, so that the expected difference between Z -factors at the corresponding physical momenta is small, one can use this observation to estimate the magnitude of the discretization error effects. It turns out that their significance varies depending on the particular operator for which the Z -factor is computed. As a result of our study we found that discretization errors are quite large for the local vector and axial currents, and even larger for the exactly conserved vector and axial currents. In the 16^4 volume, for example, only four to five points with the lowest lattice momenta have

reasonably small errors. This implies that it is virtually impossible to study the running of the renormalization coefficients for these operators without using the scaling technique or performing simulations in very large volumes that is extremely expensive computationally.

IV. NUMERICAL RESULTS

We use the fermion action which is the hermitian conjugate of the action in Ref. [5] where the domain wall fermion method was introduced. The domain wall fermion operator that we use is given by

$$D_{x,s;x',s'} = \delta_{s,s'} D_{x,x'}^{\parallel} + \delta_{x,x'} D_{s,s'}^{\perp} \quad (14)$$

$$D_{x,x'}^{\parallel} = \frac{1}{2} \sum_{\mu} \left[(1 - \gamma_{\mu}) U_{x,\mu} \delta_{x+\hat{\mu},x'} + (1 + \gamma_{\mu}) U_{x',\mu}^{\dagger} \delta_{x-\hat{\mu},x'} \right] + (M_5 - 4) \delta_{x,x'} \quad (15)$$

$$D_{s,s'}^{\perp} = \frac{1}{2} \left[(1 - \gamma_5) \delta_{s+1,s'} + (1 + \gamma_5) \delta_{s-1,s'} - 2\delta_{s,s'} \right] - \frac{m_f}{2} \left[(1 - \gamma_5) \delta_{s,L_s-1} \delta_{0,s'} + (1 + \gamma_5) \delta_{s,0} \delta_{L_s-1,s'} \right] \quad (16)$$

Operators are constructed from an interpolating operator for the light fermion of the form

$$q(x) = P_L \Psi_{x,0} + P_R \Psi_{x,L_s-1} \quad (17)$$

$$\bar{q}(x) = \bar{\Psi}_{x,0} P_R + \bar{\Psi}_{x,L_s-1} P_L \quad (18)$$

Evaluation of the matrix elements is done in Landau gauge. The gauge is fixed on each configuration by finding a unitary transformation of the lattice links that maximizes the functional

$$\text{Tr} \sum_{\mu=1}^4 \left(U_{\mu}(x) + U_{\mu}^{\dagger}(x) \right) . \quad (19)$$

In our calculations the parameter M_5 is set to 1.8. We use lattice volumes 8^4 and 16^4 at three values of β , 6.0, 6.45, and 7.05. We assume the inverse lattice spacing at $\beta = 6.0$ to be 1.96 GeV , twice that at $\beta = 6.45$, and four times that at $\beta = 7.05$. These values are based on the string tension data in [11]. The scale for $\beta = 6.45$ was obtained by interpolating the data from that paper using the two-loop perturbation formula for the running coupling constant. The result for $\beta = 7.05$ was obtained by extrapolating and is less accurate.

The chiral limit for the local operators is taken using correlated fits to the results obtained at a set of masses $m_f = 0.004, 0.012, 0.020$ in 16^4 volume and $m_f = 0.004, 0.012, 0.020, 0.028$ in 8^4 volume.

In the case of conserved currents all simulations are performed with $m_f = 0.05$, which is small enough for the results to be in the chiral limit. We tested this statement by repeating one of the points using $m_f = 0.02$ and found the data to be in agreement within statistical errors.

A. Local Vector and Axial Currents

Now we present the results for renormalization coefficients of local vector and axial currents. The local vector and axial current densities are defined by

$$V_L^\mu(x) = \bar{q}\gamma^\mu q(x) \quad (20)$$

and

$$A_L^\mu(x) = \bar{q}\gamma^\mu\gamma_5 q(x) . \quad (21)$$

In these equations flavor non-singlet currents are implied. The flavor index is suppressed to simplify the notation. The matrix elements of the vector and axial currents in external quark states include finite terms that depend on the direction of the external momentum in addition to the term proportional to the free-field vertex. In the continuum the form of these matrix elements is the following,

$$\Lambda_{V^L}^\mu(p) = A_{V^L}(p^2)\gamma^\mu + B_{V^L}(p^2)\frac{p^\mu\not{p}}{p^2} \quad (22)$$

and

$$\Lambda_{A^L}^\mu(p) = A_{A^L}(p^2)\gamma^\mu\gamma_5 + B_{A^L}(p^2)\frac{p^\mu\not{p}}{p^2}\gamma_5 . \quad (23)$$

For the Z -factors we use the definition with the four Lorentz components of matrix elements combined by contracting with the gamma matrices,

$$\frac{Z_q(\mu; a)}{Z_{V^L}(\mu; a)} \equiv \frac{1}{48} \text{Tr} \left(\Lambda_{V^L}^\mu(p; a)\gamma^\mu \right)_{p^2=\mu^2} \quad (24)$$

and

$$\frac{Z_q(\mu; a)}{Z_{A^L}(\mu; a)} \equiv \frac{1}{48} \text{Tr} \left(\Lambda_{A^L}^\mu(p; a)\gamma^\mu\gamma_5 \right)_{p^2=\mu^2} . \quad (25)$$

With these definitions the second term in Eqs. (22) and (23) with coefficient $B(p^2)$ is included as part of the matrix element. (Alternatively, one could separate the coefficient of the term proportional to the free-field vertex, for example, by tracing the $\mu = 0$ component of the matrix element calculated at momenta p with $p^0 = 0$ with γ^0 for the vector current and $\gamma^0\gamma_5$ for the axial current.)

Figure 2 shows the renormalization coefficients Z_q/Z_{V^L} and Z_q/Z_{A^L} versus the energy scale μ in GeV in the chiral limit. The rows correspond to different physical volumes. The pairs of points on each plot in the two lower rows are from simulations at pairs of different β 's with the lattice spacing differing by factors of two. Since the number of lattice sites differs by the inverse of two, the physical volumes are the same.

Figure 3 demonstrates the procedure of obtaining the rescaling coefficients R_A and R_V for two pairs of β , 6.45, 6.0 and 7.05, 6.45. Each point in Figure 3 is a ratio of the Z -factors in Figure 2 determined at the same physical momentum and in the same physical volume.

There are four ratios at each pair of β 's, since we only use the lowest four momenta in 8^4 lattice volume (triangular symbols in Figure 2).

As described in Section III, these ratios would be μ independent in the absence of discretization errors. With finite lattice spacing these errors are quadratic in momentum scale μ , see Eq. (11). In order to remove the effects of discretization errors, we extrapolate the ratios linearly in μ^2 to $\mu \rightarrow 0$, Figure 3. The rescaling coefficients for the local vector and axial density operators turn out to be very close to one.

Finally, using the rescaling coefficients we rescale the renormalization coefficients according to Eq. (13) so that they are all defined with the same ultraviolet cutoff, determined by the lattice spacing at $\beta = 7.05$. The results are shown in Figure 4. There is a pretty good agreement between the data computed in different physical volumes at low lattice momenta (the first few low momentum points on each graph) that indicates small finite volume effects for local vector and axial current data. At the same time, discretization errors start effecting data pretty early. To emphasize the actual behavior of the Z -factors we use solid symbols for the points that have relatively small discretization errors. These are the same points that are used in calculating the rescaling coefficients in Figure 3.

The renormalization group running of Z_q from perturbative analysis [12] is represented by a solid line. This line is defined up to an overall multiplicative constant that we do not determine. Instead, we choose it so that the line agrees with our numerical data at scales about 10 GeV. The coefficient Z_{VL} should be momentum-independent. It reflects the renormalization of the local vector current relative to the exactly conserved on the lattice vector current whose renormalization coefficient is equal to one according to the Ward Identity, Section IV C. The two currents are different at the scales of order a^{-1} , while for the scales $\mu \ll a^{-1}$ the difference can be absorbed into Z_{VL} . Therefore, the dependence of Z_q/Z_{VL} on the scale μ should be the same as the dependence of Z_q itself. There is a good agreement between the RG line and the data for Z_q/Z_{VL} in the whole range of the scales. On the other hand, Z_{AL} defined by Eq. (25) is momentum-independent only at large scales μ . The reason is the same as for the difference between Z_q obtained from the conserved vector current and $Z_q^{(A)}$ from axial current, see Section IV C.

B. Scalar and Pseudoscalar operators

Now we present the results for renormalization coefficients of scalar and pseudoscalar operators. The matrix elements of the pseudoscalar density at low energy scales (about 1–2 GeV) receive contributions from the chiral symmetry breaking in the form of a pole in momentum squared and quark mass,

$$\Lambda_P(p^2) = \frac{Z_q(p^2)}{Z_P(p^2)} + \frac{C \langle \bar{q}q \rangle}{p^2 m_f}. \quad (26)$$

The general form of the chiral condensate is given by the equation

$$\langle \bar{q}q \rangle = a + bm_f + \frac{c}{m_f \sqrt{V}} \quad (27)$$

The third term in the above equation is due to the fermion zero modes present in our quenched simulations, Ref. [13]. This term, which is inversely proportional to m_f , is suppressed by the square root of the volume and is small in comparison with the constant term for the parameters used in our simulations. Therefore, in Eq. (26) for the pseudoscalar density the mass dependence of the second term is very well described by the equation

$$\frac{C_1}{p^2 m_f}. \quad (28)$$

For the scalar density we have,

$$\Lambda_S(p^2) = \frac{Z_q(p^2)}{Z_S(p^2)} + \frac{C}{p^2} \frac{\partial \langle \bar{q}q \rangle}{\partial m_f}. \quad (29)$$

In this case the constant term in the chiral condensate, Eq. (27), is removed by the derivative. Therefore, the third term in Eq. (27) which is inversely proportional to m_f , can determine the form of the mass-dependence of Λ_S in small physical volumes. In this case the contribution to $\Lambda_S(p^2)$ from the second term in Eq. (29) has the form

$$- \frac{1}{m_f^2} \frac{C_2}{p^2}. \quad (30)$$

When taking the chiral limit of scalar and pseudoscalar densities at energy scales of a few GeV in finite volume, one needs to remove these non-leading, $1/p^2$ contributions which have singular behavior as $m_f \rightarrow 0$. For a thorough discussion of both of these effects see [14].

The presence of these terms is clearly seen in Figure 5 where the data for a 16^4 volume at $\beta = 6.0$ for a set of quark masses is presented. Their contribution to the scalar density becomes significant only for $m_f = 0.004$ and is almost invisible for $m_f = 0.02$. Figure 6 shows results at $\beta = 6.45$. At this β there is little evidence of such small- m_f divergent term, which is consistent with the absence of the chiral symmetry breaking in this smaller physical volume.

Figure 7 shows the renormalization coefficients Z_q/Z_P and Z_q/Z_S plotted versus the energy scale μ in GeV in the chiral limit. To obtain these results, we performed correlated fits in m_f at each momentum in the form Eqs. (28) and (30) plus finite, m_f -independent renormalization coefficients Z_q/Z_P and Z_q/Z_S . The arrangement of the graphs is the same as for the local vector and axial currents.

The result of the scaling procedure is shown in Figure 8. Solid lines are the renormalization group running from a 3-loop perturbation theory analysis, [12]. They represent the evolution of the Z -factors with the energy scale, and are defined up to an overall multiplicative constant which we do not determine. We choose this constant to match the RG curve with our data at large scales μ around 10 GeV. The data exhibits large finite volume effects at small momenta in each of the three different physical volumes. This results in the difference between data at the corresponding momenta obtained in different volumes. This difference vanishes as the momentum scale becomes large within the individual momentum range for each volume. On the other hand, discretization error effects are barely noticeable.

C. Conserved Vector and Axial Currents

The exactly conserved domain wall vector and axial currents can be used to compute Z_q . Following Ref. [15], with our fermion operator given by Eq. (14) these currents are defined by the equation

$$J_\mu(x) = \sigma_J \sum_{s=0}^{L_s/2-1} j_\mu(x, s) + \sum_{s=L_s/2}^{L_s-1} j_\mu(x, s), \quad (31)$$

where $J = V$ or A and $\sigma_V = +1$, $\sigma_A = -1$ and

$$j_\mu(x, s) = \bar{\Psi}_{x+\hat{\mu},s} \frac{1 + \gamma_\mu}{2} U_\mu^\dagger(x) \Psi_{x,s} - \bar{\Psi}_{x,s} \frac{1 - \gamma_\mu}{2} U_\mu(x) \Psi_{x+\hat{\mu},s}. \quad (32)$$

Here flavor non-singlet currents are implied with the flavor indices suppressed for simplicity of notation. With the definition of Z_q given by Eq. (6) we can use the Ward Identity Eq. (7) for the exactly conserved vector current which implies Eq. (8). The corresponding Ward Identity for the axial current has an additional term that does not vanish in the chiral limit, due to the presence of a massless Goldstone boson. It becomes negligible at sufficiently large scales μ (see a proof in [3] for example). For this reason, when we apply the same equation Eq. (8) with Λ_{AC}^μ , the resulting renormalization coefficient $Z_q^{(A)}$ is different from Z_q when evaluated at scales below ~ 2 GeV.

Due to the presence of the fermion fields at separate space-time points in Eqs. (31) and (32), propagators must be evaluated for sources at different points on the four-dimensional lattice. In addition, the summation over the position in the fifth dimension implies that propagators for all of these positions should in principle be calculated. Therefore, the calculation of the matrix elements of conserved currents can be very expensive. To minimize the amount of computational time, we use a random source estimator to compute the part of the sum between $s = 1$ and $s = L_s - 2$, with propagators for $s = 0$ and $s = L_s - 1$ calculated explicitly. Also, instead of calculating all four components of $\Gamma^\mu(p)$ for a given momentum p , we calculate $\Gamma^0(p)$ for momenta related to p by permuting its 0th component with the rest of the components,

$$\begin{aligned} \text{Tr} \left(\gamma^\mu \Gamma^\mu(p^0, p^1, p^2, p^3) \right) &= \text{Tr} \left(\gamma^0 \Gamma^0(p^0, p^1, p^2, p^3) \right) + \text{Tr} \left(\gamma^0 \Gamma^0(p^1, p^0, p^2, p^3) \right) \\ &+ \text{Tr} \left(\gamma^0 \Gamma^0(p^2, p^1, p^0, p^3) \right) + \text{Tr} \left(\gamma^0 \Gamma^0(p^3, p^1, p^2, p^0) \right). \end{aligned} \quad (33)$$

The computer time required to Fourier transform a matrix element is negligible in comparison with the calculation of the matrix element itself, therefore the formula above allows us to obtain the result with only a quarter of the running time.

We used $m_f = 0.05$ in our simulations for the conserved vector and axial currents which from our experience is sufficiently close to the chiral limit. A test run at $\beta = 6.0$ with $m_f = 0.02$ with 30 configurations produced results consistent within statistical errors. In Figure 9 we plot Z_q computed from the conserved vector current using Eqs. (8) and (33). The same figure shows the renormalization coefficient $Z_q^{(A)}$ obtained by applying these equations with the axial current.

The data is similar to that obtained for the local vector and axial currents, but shows larger discretization errors. In Figure 10 we plot the evolution of Z_q and $Z_q^{(A)}$ factors computed from the conserved vector and axial currents after rescaling, such that the ultraviolet cutoff is equal to the lattice spacing at $\beta = 7.05$. The renormalization group running of Z_q from a perturbative analysis [12] is represented by a solid line. This line is defined up to an overall multiplicative constant that we do not determine. Instead, we choose it so that the line agrees with our numerical data at scales about 10 GeV.

From the results in Figure 10 obtained at different β 's, one can see that while the finite volume effects are still small, as in the local current case, the quadratic in μa deviations due to discretization errors that curves the results up become significant very early. Essentially, only the first five points with lowest momenta at each β seem to have relatively small discretization errors. This statement of course is correct only in a 16^4 volume. But it does suggest that attempts to analyze the momentum dependence of Z_q from conserved currents using simulations at a single value of β are subject to large discretization errors. We use solid symbols for the data points that have reasonable discretization errors. These are the same points that are used in calculating the rescaling coefficients for conserved currents.

The results from the conserved vector and axial currents agree pretty well at the scales of about 2 GeV and above. At the same time, at 2 GeV and below there is large difference between Z_q and $Z_q^{(A)}$. The difference reaches almost 20% at about 1 GeV and is more than 30% at 0.8 GeV. The numerical results therefore indicate that the additional finite term in the axial Ward Identity is large at these scales. The same argument is consistent with the data for the rescaling coefficients in Table I. The agreement between rescaling coefficients for Z_q and $Z_q^{(A)}$ is much better for the pair of weaker couplings $\beta = 6.45$ and $\beta = 7.05$ than for $\beta = 6.0$ and $\beta = 6.45$.

The results in Figure 10 are in poor agreement with the renormalization group curve from perturbation theory, though it becomes slightly better at large momenta as the scale dependence of Z_q (and $Z_q^{(A)}$) becomes flatter. This is in sharp contrast with the results for the local vector and axial currents, Figure 4. In the absence of scaling violations the results from local currents should agree up to an overall momentum-independent factor with the results from the conserved currents, as argued in Section IV A. We interpret this inconsistency between our results for the local and conserved currents as arising from discretization errors present in the non-local, conserved currents. These can arise in two ways. First, our matching procedure using the small 8^4 volumes might not be able to properly account for the order $O(a^2\mu^2)$ terms. This difficulty can be addressed by working on 16^4 and 32^4 volumes that would allow smaller lattice momenta to be used, therefore reducing the errors. The second source of errors may arise from the failure of these non-local conserved currents to scale at couplings as strong as $\beta = 6.0$.

D. B_K

In this section we present the results of non-perturbative renormalization of a phenomenologically important parameter B_K which is relevant to the calculation of the $K^0 - \bar{K}^0$ mixing amplitude. The standard definition of B_K is given by

$$B_K(\mu) = \frac{\langle \bar{K}^0 | O_{LL}^{\Delta S=2}(\mu) | K^0 \rangle}{\langle \bar{K}^0 | O_{LL}^{\Delta S=2}(\mu) | K^0 \rangle_{VSA}} = \frac{\langle \bar{K}^0 | O_{LL}^{\Delta S=2}(\mu) | K^0 \rangle}{\frac{8}{3} f_K^2 m_K^2}. \quad (34)$$

This definition implies that B_K renormalizes in the same way as the four-fermion operator

$$O_{LL}^{\Delta S=2} = \left(\bar{s} \gamma^\mu \frac{1 - \gamma_5}{2} d \right) \left(\bar{s} \gamma^\mu \frac{1 - \gamma_5}{2} d \right) \equiv \bar{s} \gamma_L^\mu d \bar{s} \gamma_L^\mu d. \quad (35)$$

We closely follow the RI procedure for renormalization of this operators described in [16]. In the domain wall fermion formulation the mixing with operators of different chiralities is small and is not studied in our paper. For more detailed treatment of this topic the reader is referred to Ref. [8]. The four-point Green's function is defined by

$$G_{B_K}(x_1, x_2, x_3, x_4) = \langle s(x_1) \bar{d}(x_2) O_{LL}^{\Delta S=2}(0) s(x_3) \bar{d}(x_4) \rangle. \quad (36)$$

For the Fourier transformed Green's function the off-shell external momenta are chosen to be equal. Using the upper Roman indices to denote color and the lower Greek indices to denote spin, the non-amputated Green's function can be written as

$$G_{B_K}(p)_{\alpha\beta\gamma\delta}^{ABCD} = 2 \left[\langle \Gamma^\mu(p)_{\alpha\beta}^{AB} \Gamma^\mu(p)_{\gamma\delta}^{CD} \rangle - \langle \Gamma^\mu(p)_{\alpha\delta}^{AD} \Gamma^\mu(p)_{\gamma\beta}^{CB} \rangle \right], \quad (37)$$

where

$$\Gamma^\mu(p)_{\alpha\beta}^{AB} = S(p|0)_{\alpha\sigma}^{AR} \gamma_{L\sigma\rho}^\mu \left(\gamma_5 S(p|0)^\dagger \gamma_5 \right)_{\rho\beta}^{RB}. \quad (38)$$

$S(p|0)$ is a Fourier transformed propagator on a single configuration in Landau gauge. It is not translationally invariant.

The amputated Green's function is calculated from the non-amputated one by multiplying it with the inverse propagator $S(p)$ averaged over all configurations

$$\Lambda_{B_K}(p)_{\alpha\beta\gamma\delta}^{ABCD} = S^{-1}(p)_{\alpha\alpha'}^{AA'} S^{-1}(p)_{\gamma\gamma'}^{CC'} G_{B_K}(p)_{\alpha'\beta'\gamma'\delta'}^{A'B'C'D'} S^{-1}(p)_{\beta'\beta}^{B'B} S^{-1}(p)_{\delta'\delta}^{D'D}. \quad (39)$$

The projection operation Eq. (4) is defined by the equation

$$\Gamma_{B_K}(p; a) = \frac{1}{32 N_c (N_c + 1)} \gamma_{L\alpha\alpha'}^\mu \gamma_{L\beta\beta'}^\mu \Lambda_{B_K}(p)_{\alpha'\alpha\beta'\beta}^{AABB}, \quad (40)$$

where $N_c = 3$ is the number of colors. The renormalization condition imposed on the $O^{\Delta S=2}$ operator is given by the same formula Eq. (2).

The numerical results for this Z -factor obtained with different values of m_f have no statistically significant dependence on m_f . Nevertheless, the same procedure of linear correlated fitting in m_f was applied to take the chiral limit with the results shown in Figure 11. The final results after rescaling to a new ultraviolet cutoff equal to the lattice spacing at $\beta = 7.05$ are presented in Figure 12. It is interesting to notice that the finite volume effects at low lattice momenta are very significant and for the lowest momenta are of the order of 50%. This same volume dependence can also be seen from a direct comparison with the smaller, 8^4 volume at the same β . For illustration purposes we include the result at $\beta = 6.0$ in a 8^4 volume in Figure 12 using small circles. The data points for this smaller volume are

rescaled using the same factor as the $\beta = 6.0$, 16^4 volume result, therefore the difference between the two results is a direct result of the finite volume effects. The systematic difference from the data at $\beta = 6.45$ that has the same physical volume is due to larger discretization errors that are present in the $\beta = 6.0$ data at the corresponding momenta.

The solid line on the graph is for the one-loop renormalization group analysis in perturbation theory [17]. Since it is defined up to an overall multiplicative constant which we do not determine, we matched it with the numerical result at large energy scales μ of about 10 GeV. There is a surprisingly good agreement in the whole range from 1 to 10 GeV. This might be fortuitous for μ lower than 2 GeV, since at these scales we expect large non-perturbative effects. These effects together with the large finite volume effects at low momenta could have resulted in the flat shape of numerical results at around 1 GeV.

V. CONCLUSIONS

The combination of recursive scaling and NPR offers a promising connection between the perturbative and non-perturbative regimes—a connection that is required if perturbative errors are to be properly controlled. The results reported here suggest a consistent picture for the scaling of renormalization factors over a momentum range between 2 and 10 GeV for the case of quenched domain wall fermions for the operators analyzed. The only exception to this generally satisfactory picture occurs in the comparison of the local and conserved currents, where the larger discretization errors present in the non-local, conserved currents may be at fault. To fully resolve this issue and demonstrate the validity of this approach more extensive calculations and larger lattice volumes will be required.

VI. ACKNOWLEDGMENTS

The author thanks C. Dawson for much important assistance with the NPR technique and N. Christ, T. Blum, and R. Mawhinney for helpful discussions, and other collaborators and Columbia and Brookhaven for the hardware and software resources which were essential to this work.

All of the numerical calculations were done on the 400 Gflops QCDSF computer at Columbia University and the 600 Gflops QCDSF computer at the RIKEN-BNL Research Center. This work was supported in part by the U.S. Department of Energy and the RIKEN BNL Research Center.

REFERENCES

- [1] G. Parisi, High Energy Physics–1980 proceedings of the XX International Conference, Madison, Wisconsin
- [2] G. P. Lepage and P. B. Mackenzie, Phys. Rev. **D48**, 2250 (1993), hep-lat/9209022.
- [3] G. Martinelli, C. Pittori, C. T. Sachrajda, M. Testa and A. Vladikas, Nucl. Phys. **B445**, 81 (1995), hep-lat/9411010.
- [4] D. B. Kaplan, Nucl. Phys. Proc. Suppl. **30**, 597 (1993)
- [5] Y. Shamir, Nucl. Phys. **B406**, 90 (1993), hep-lat/9303005.
- [6] R. Narayanan and H. Neuberger, Nucl. Phys. **B443**, 305 (1995), hep-th/9411108.
- [7] P. Vranas, hep-lat/0011066.
- [8] C. Dawson [RBC Collaboration], hep-lat/0011036.
- [9] T. Blum *et al.*, hep-lat/0007038.
- [10] A. Ali Khan *et al.* [CP-PACS Collaboration], hep-lat/0007014.
- [11] G. S. Bali and K. Schilling, Phys. Rev. **D47**, 661 (1993), hep-lat/9208028.
- [12] K. G. Chetyrkin and A. Retey, Nucl. Phys. **B583**, 3 (2000), hep-ph/9910332.
- [13] M. Wingate *et al.* [RIKEN-BNL-CU Collaboration], hep-lat/0009022.
- [14] T. Blum *et al.*, in preparation.
- [15] V. Furman and Y. Shamir, Nucl. Phys. **B439**, 54 (1995), hep-lat/9405004.
- [16] A. Donini, G. Martinelli, C. T. Sachrajda, M. Talevi and A. Vladikas, Phys. Lett. **B360**, 83 (1995), hep-lat/9508020.
- [17] M. Ciuchini, E. Franco, V. Lubicz, G. Martinelli, I. Scimemi and L. Silvestrini, Nucl. Phys. **B523**, 501 (1998), hep-ph/9711402.

TABLES

TABLE I. Rescaling coefficients.

Z -factor	$R(a(\beta = 6.45), a(\beta = 6.0))$	$R(a(\beta = 7.05), a(\beta = 6.45))$
Z_q/Z_{VL}	1.016(3)	0.999(2)
Z_q/Z_{AL}	1.014(3)	0.987(2)
Z_q/Z_P	1.088(9)	1.039(6)
Z_q/Z_S	1.046(8)	1.025(6)
$Z_q^2/Z_{O_{LL}^{\Delta S=2}}$	0.881(9)	0.932(8)
Z_q	1.188(13)	1.067(5)
$Z_q^{(A)}$	1.092(13)	1.047(5)

TABLE II. Z -factors at $\beta = 6.0$ in 16^4 lattice volume. The mass for the local Z -factors is $m_f = 0.02$, while for the conserved currents (last two columns) $m_f = 0.05$.

$p_i a$	μ, GeV	Z_q/Z_{VL}	Z_q/Z_{AL}	Z_q/Z_P	Z_q/Z_S	$Z_q^2/Z_{O_{LL}^{\Delta S=2}}$	Z_q	$Z_q^{(A)}$
0001	0.770	1.1859(91)	0.9865(71)	5.610(22)	1.43(14)	1.229(25)	0.914(16)	0.748(12)
0011	1.089	1.1350(48)	1.0545(39)	3.620(13)	1.430(89)	1.258(15)	0.862(13)	0.790(11)
0111	1.333	1.1142(41)	1.0731(35)	2.799(89)	1.451(65)	1.265(13)	0.841(12)	0.801(12)
0002	1.539	1.0882(27)	1.0660(26)	2.361(66)	1.466(50)	1.238(10)	0.824(14)	0.800(14)
1111	1.539	1.1034(45)	1.0820(45)	2.314(54)	1.456(37)	1.273(15)	0.828(11)	0.802(10)
0012	1.721	1.0915(23)	1.0749(21)	2.081(48)	1.432(36)	1.249(9)	0.836(10)	0.817(10)
0112	1.885	1.0917(25)	1.0804(23)	1.907(36)	1.419(25)	1.261(9)	0.841(11)	0.828(11)
1112	2.036	1.0927(29)	1.0836(29)	1.785(28)	1.405(18)	1.271(10)	0.844(12)	0.836(12)
0022	2.177	1.0913(22)	1.0835(21)	1.703(24)	1.386(16)	1.268(8)	0.873(10)	0.863(10)
0122	2.309	1.0938(24)	1.0880(24)	1.639(22)	1.370(15)	1.282(9)	0.888(10)	0.881(10)
1122	2.434	1.0962(29)	1.0913(29)	1.591(18)	1.364(12)	1.292(10)	0.902(11)	0.897(11)
0222	2.666	1.1004(27)	1.0966(27)	1.522(16)	1.339(12)	1.307(10)	0.958(11)	0.953(11)
1222	2.775	1.1025(32)	1.0993(32)	1.497(13)	1.344(10)	1.315(11)	0.977(12)	0.971(12)
2222	3.079	1.1100(36)	1.1079(36)	1.441(10)	1.328(09)	1.342(13)	1.057(14)	1.053(14)

TABLE III. Rescaled Z -factors in the chiral limit versus the energy scale. The Z -factors in this table are defined with the ultraviolet cutoff equal to the lattice spacing at $\beta = 7.05$. The physical extent of the lattice in each dimension is 16 times the lattice spacing at $\beta = 6.0$.

μ, GeV	Z_q/Z_{VL}	Z_q/Z_{AL}	Z_q/Z_P	Z_q/Z_S	$Z_q^2/Z_{O_{LL}^{\Delta S=2}}$	Z_q	$Z_q^{(A)}$
0.770	1.1910(15)	1.0045(12)	2.1989(147)	2.0848(78)	1.0188(34)	1.1591(24)	0.8554(18)
1.089	1.1533(8)	1.0691(7)	1.9869(79)	1.8985(47)	1.0521(21)	1.0939(21)	0.9034(17)
1.333	1.1309(7)	1.0831(6)	1.8653(55)	1.7918(37)	1.0500(19)	1.0668(20)	0.9167(18)
1.539	1.1014(5)	1.0726(5)	1.7911(38)	1.7010(29)	1.0202(17)	1.0447(22)	0.9153(20)
1.539	1.1200(7)	1.0903(7)	1.8335(40)	1.7317(28)	1.0487(22)	1.0500(19)	0.9171(17)
1.721	1.1069(5)	1.0815(5)	1.7470(31)	1.6485(23)	1.0294(16)	1.0598(18)	0.9347(17)
1.885	1.1076(5)	1.0857(5)	1.6891(27)	1.6035(21)	1.0389(16)	1.0662(18)	0.9466(17)
2.036	1.1082(5)	1.0864(5)	1.6466(24)	1.5668(21)	1.0459(17)	1.0707(20)	0.9563(18)
2.177	1.1074(5)	1.0880(5)	1.6230(21)	1.5363(18)	1.0445(16)	1.1067(18)	0.9870(17)
2.309	1.1098(5)	1.0916(5)	1.5988(20)	1.5142(17)	1.0557(16)	1.1268(19)	1.0076(17)
2.434	1.1127(5)	1.0942(5)	1.5776(20)	1.4973(17)	1.0636(17)	1.1446(20)	1.0255(18)
2.666	1.1169(5)	1.0989(5)	1.5500(18)	1.4673(16)	1.0755(17)	1.2148(20)	1.0895(18)
2.775	1.1186(5)	1.1013(5)	1.5393(18)	1.4635(16)	1.0812(17)	1.2391(21)	1.1108(20)
3.079	1.1268(6)	1.1103(6)	1.5212(18)	1.4394(16)	1.1040(18)	1.3404(23)	1.2039(22)

TABLE IV. Rescaled Z -factors in the chiral limit versus the energy scale. The Z -factors in this table are defined with the ultraviolet cutoff equal to the lattice spacing at $\beta = 7.05$. The physical extent of the lattice in each dimension is 16 times the lattice spacing at $\beta = 6.45$.

μ, GeV	Z_q/Z_{VL}	Z_q/Z_{AL}	Z_q/Z_P	Z_q/Z_S	$Z_q^2/Z_{O_{LL}^{\Delta S=2}}$	Z_q	$Z_q^{(A)}$
1.539	1.1052(6)	1.0861(6)	2.2889(33)	2.0970(37)	1.3771(25)	0.9897(17)	0.8713(13)
2.177	1.0782(3)	1.0634(3)	1.7676(18)	1.7055(19)	1.1810(14)	0.9178(12)	0.8718(11)
2.666	1.0699(3)	1.0553(3)	1.5857(14)	1.5470(15)	1.1400(13)	0.8827(12)	0.8522(11)
3.079	1.0595(3)	1.0457(3)	1.4952(13)	1.4609(13)	1.1045(11)	0.8665(12)	0.8419(12)
3.079	1.0654(4)	1.0502(4)	1.5136(13)	1.4818(13)	1.1204(14)	0.8709(10)	0.8462(10)
3.442	1.0596(3)	1.0458(3)	1.4524(11)	1.4244(11)	1.1090(11)	0.8665(9)	0.8442(9)
3.771	1.0609(3)	1.0478(3)	1.4101(10)	1.3840(10)	1.1142(12)	0.8667(10)	0.8461(10)
4.073	1.0635(4)	1.0504(3)	1.3793(10)	1.3586(10)	1.1215(13)	0.8719(11)	0.8520(11)
4.354	1.0623(3)	1.0485(3)	1.3663(9)	1.3415(10)	1.1160(11)	0.8797(9)	0.8603(9)
4.618	1.0654(3)	1.0517(3)	1.3484(9)	1.3261(9)	1.1264(12)	0.8906(10)	0.8717(9)
4.868	1.0684(4)	1.0550(4)	1.3336(9)	1.3135(9)	1.1358(13)	0.9050(11)	0.8862(11)
5.333	1.0717(3)	1.0580(3)	1.3150(9)	1.2969(9)	1.1466(13)	0.9365(10)	0.9176(10)
5.550	1.0751(4)	1.0613(4)	1.3110(9)	1.2904(9)	1.1575(14)	0.9572(12)	0.9382(12)
6.158	1.0823(4)	1.0688(4)	1.2990(8)	1.2806(9)	1.1798(15)	1.0215(13)	1.0018(13)

TABLE V. Rescaled Z -factors in the chiral limit versus the energy scale. The Z -factors in this table are defined with the ultraviolet cutoff equal to the lattice spacing at $\beta = 7.05$. The physical extent of the lattice in each dimension is 16 times the lattice spacing at $\beta = 7.05$.

μ, GeV	Z_q/Z_{VL}	Z_q/Z_{AL}	Z_q/Z_P	Z_q/Z_S	$Z_q^2/Z_{O_{LL}^{\Delta S=2}}$	Z_q	$Z_q^{(A)}$
3.079	1.0748(8)	1.0624(4)	1.8674(28)	1.8050(30)	1.5200(28)	0.8407(12)	0.8100(12)
4.354	1.0630(2)	1.0604(2)	1.4970(13)	1.4777(13)	1.2637(12)	0.8324(8)	0.8247(8)
5.333	1.0593(2)	1.0586(2)	1.3698(9)	1.3612(9)	1.2041(10)	0.8074(8)	0.8032(8)
6.158	1.0416(1)	1.0406(1)	1.3058(8)	1.3017(8)	1.1472(5)	0.7888(7)	0.7848(7)
6.158	1.0571(3)	1.0572(3)	1.3208(7)	1.3176(7)	1.1850(11)	0.7958(8)	0.7931(8)
6.884	1.0452(1)	1.0442(1)	1.2806(5)	1.2752(5)	1.1504(5)	0.7883(7)	0.7860(7)
7.541	1.0494(2)	1.0487(2)	1.2527(5)	1.2492(5)	1.1589(5)	0.7854(6)	0.7837(6)
8.146	1.0518(2)	1.0517(2)	1.2320(5)	1.2291(5)	1.1649(7)	0.7877(7)	0.7862(7)
8.708	1.0483(1)	1.0475(1)	1.2238(4)	1.2199(4)	1.1546(4)	0.7885(6)	0.7872(6)
9.236	1.0525(2)	1.0519(2)	1.2127(4)	1.2100(4)	1.1663(6)	0.7954(6)	0.7942(6)
9.736	1.0562(2)	1.0563(2)	1.2033(4)	1.2012(4)	1.1794(8)	0.8053(7)	0.8043(7)
10.665	1.0590(2)	1.0587(2)	1.1941(4)	1.1925(4)	1.1861(7)	0.8247(6)	0.8239(6)
11.101	1.0622(3)	1.0621(3)	1.1896(4)	1.1882(4)	1.1969(9)	0.8400(7)	0.8392(7)
12.315	1.0678(3)	1.0676(3)	1.1806(4)	1.1790(4)	1.2139(11)	0.8831(8)	0.8824(8)

FIGURES

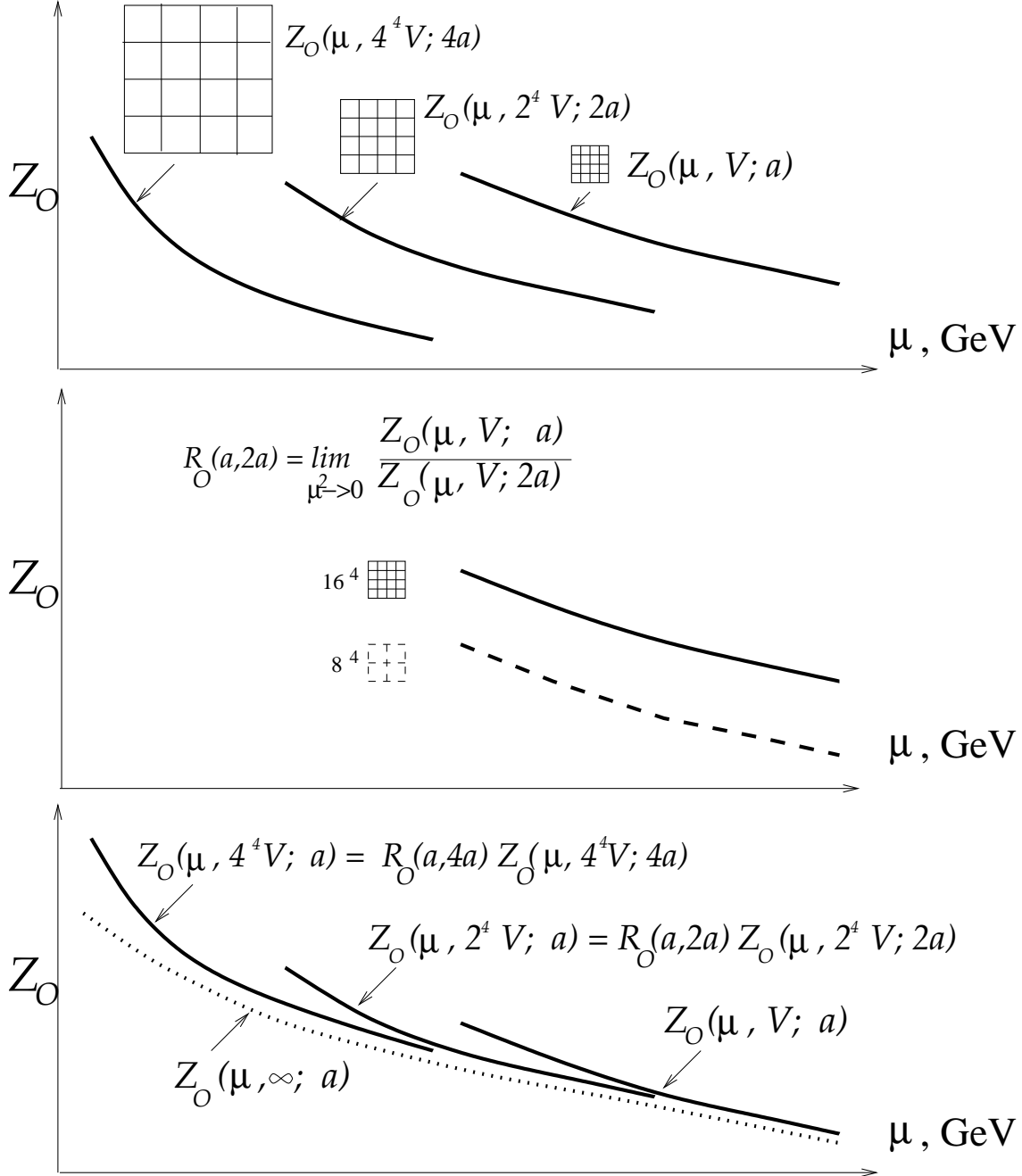


FIG. 1. Scaling procedure. Panel 1 shows Z -factors obtained at a series of different β 's and same size lattices corresponding to different physical volumes. These Z -factors cannot be meaningfully compared directly since they are defined with different values of lattice cutoff. Panel 2 shows the procedure of obtaining the rescaling coefficients R_O . Panel 3 shows Z -factors rescaled using R_O and therefore defined with the same lattice cutoff a . The ratios of the Z -factors on this graph have direct physical meaning and are cutoff-independent. Since different physical volumes are used, these Z -factors do not necessarily overlap at the corresponding momenta.

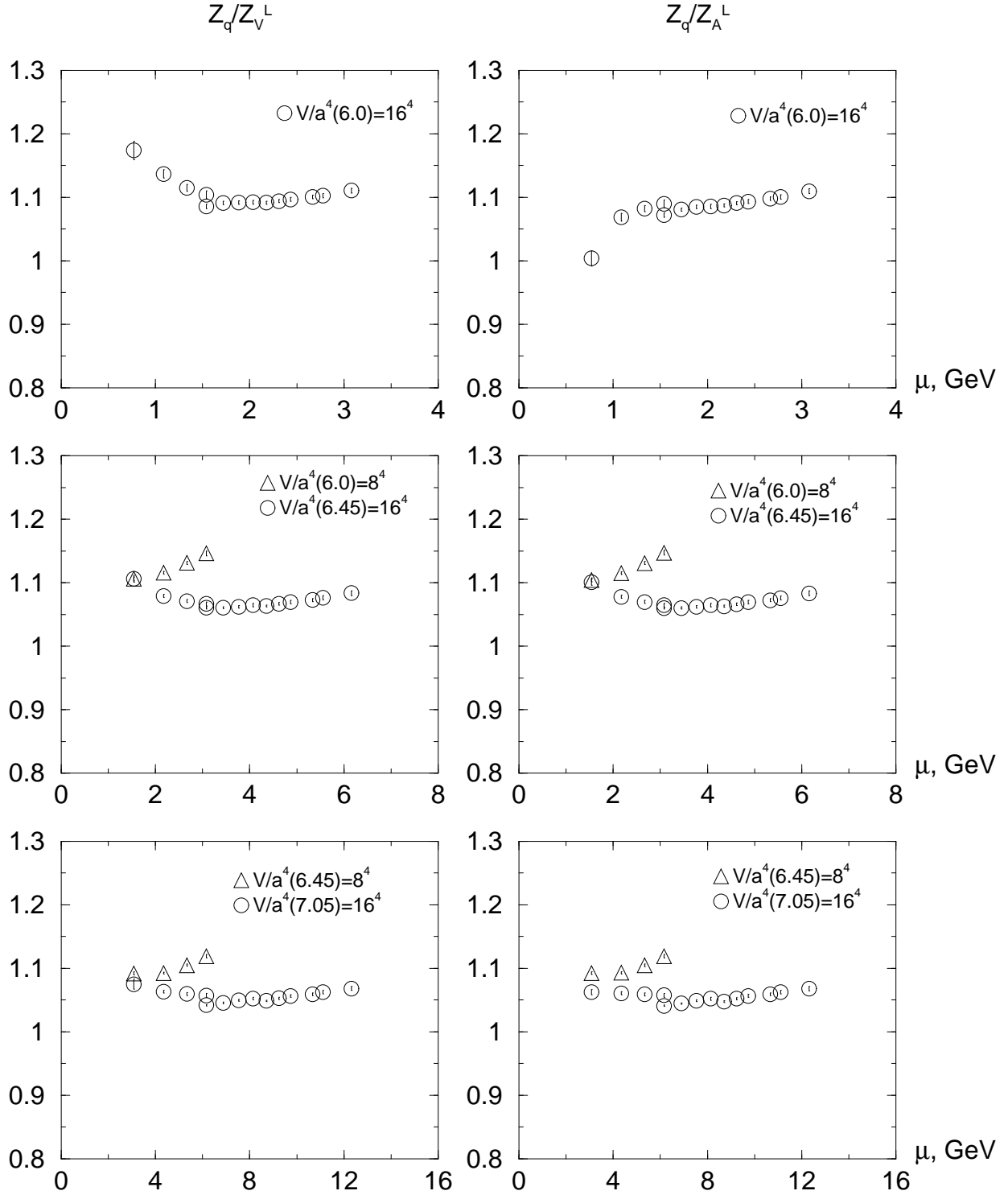
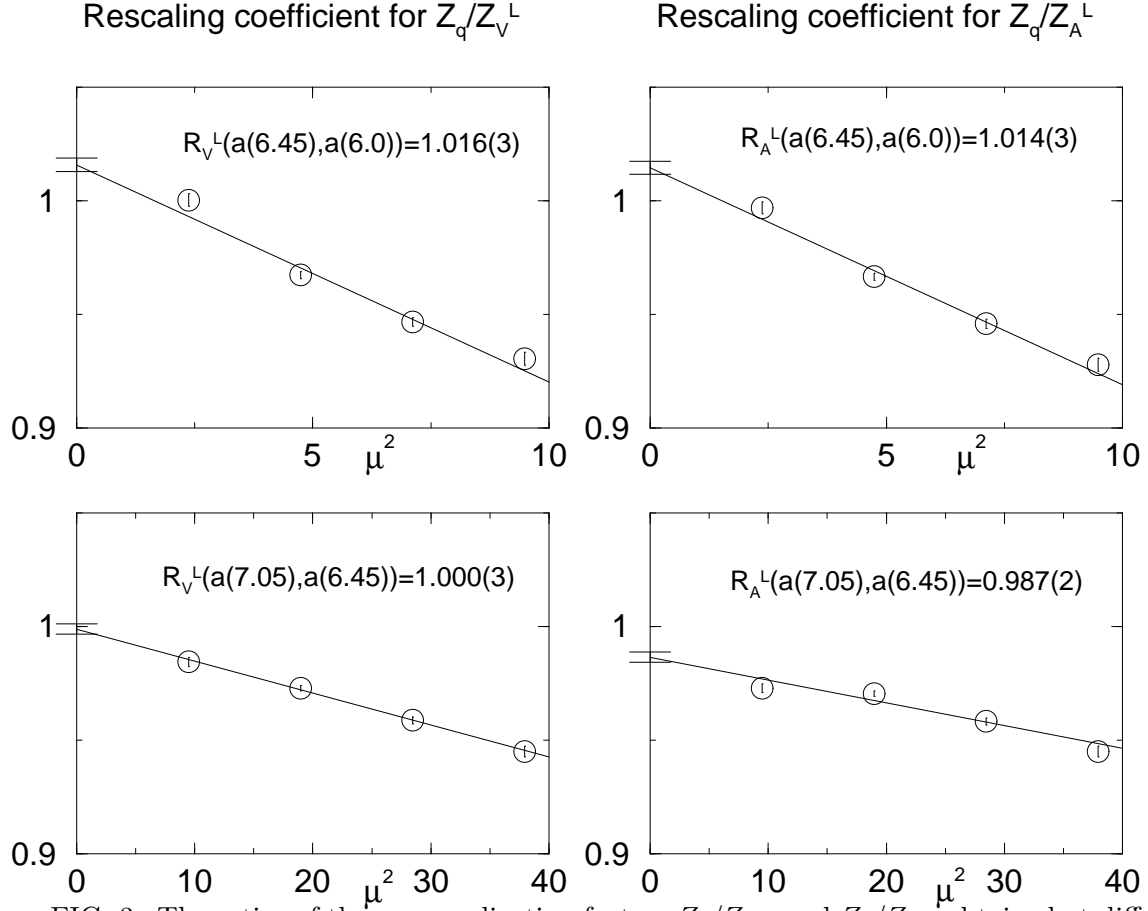


FIG. 2. Z_q/Z_{V^L} and Z_q/Z_{A^L} in the chiral limit from local vector and axial currents. Each pair of graphs is for the same physical volume.



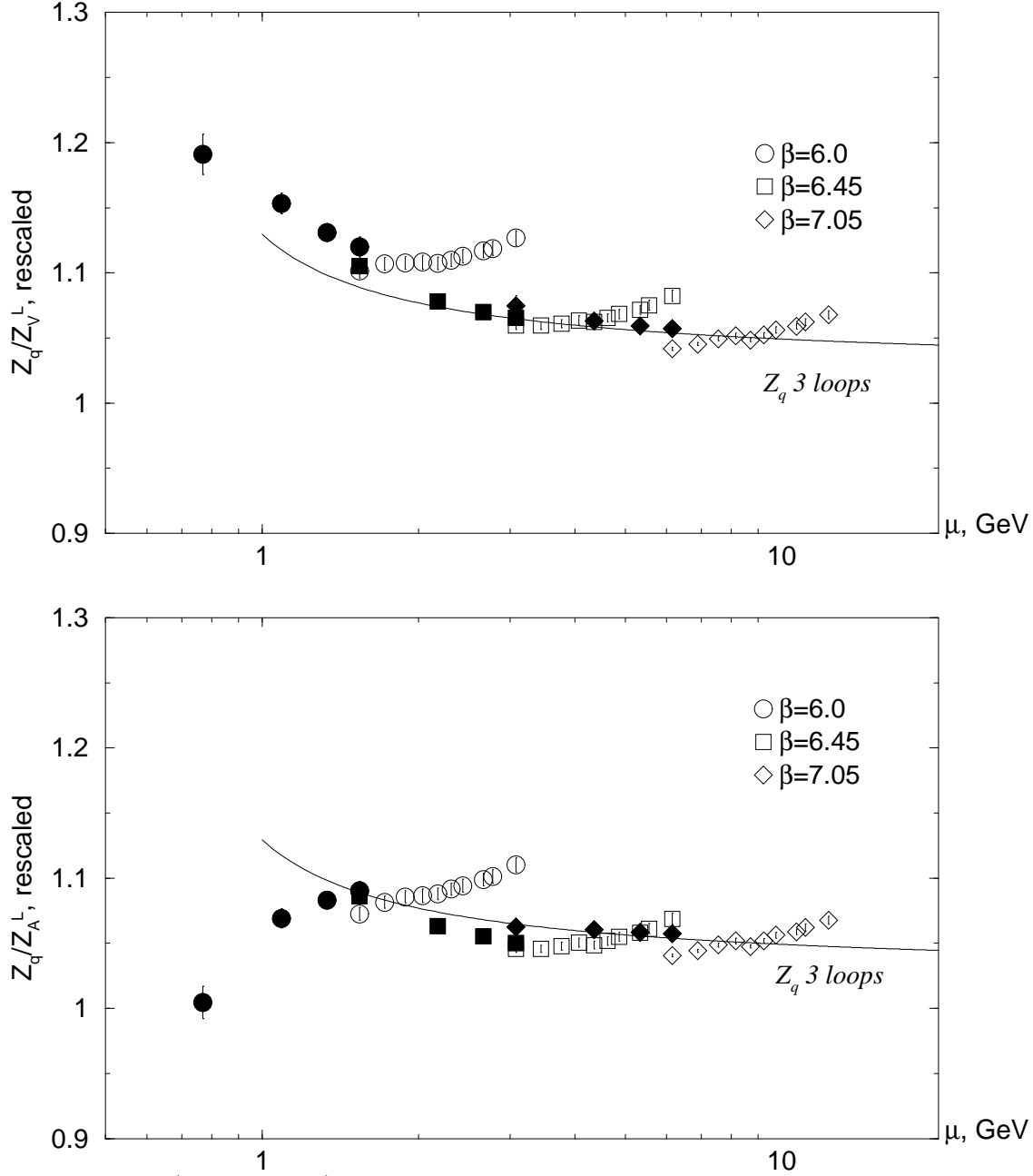


FIG. 4. Z_q/Z_{V^L} and Z_q/Z_{A^L} for local vector and axial currents in a wide range of scales μ . All graphs have the same ultraviolet cutoff equal to the lattice spacing at $\beta = 7.05$. Different symbols correspond to data in different physical volumes (labeled by β at which they are obtained). Solid symbols are for data with small discretization errors.

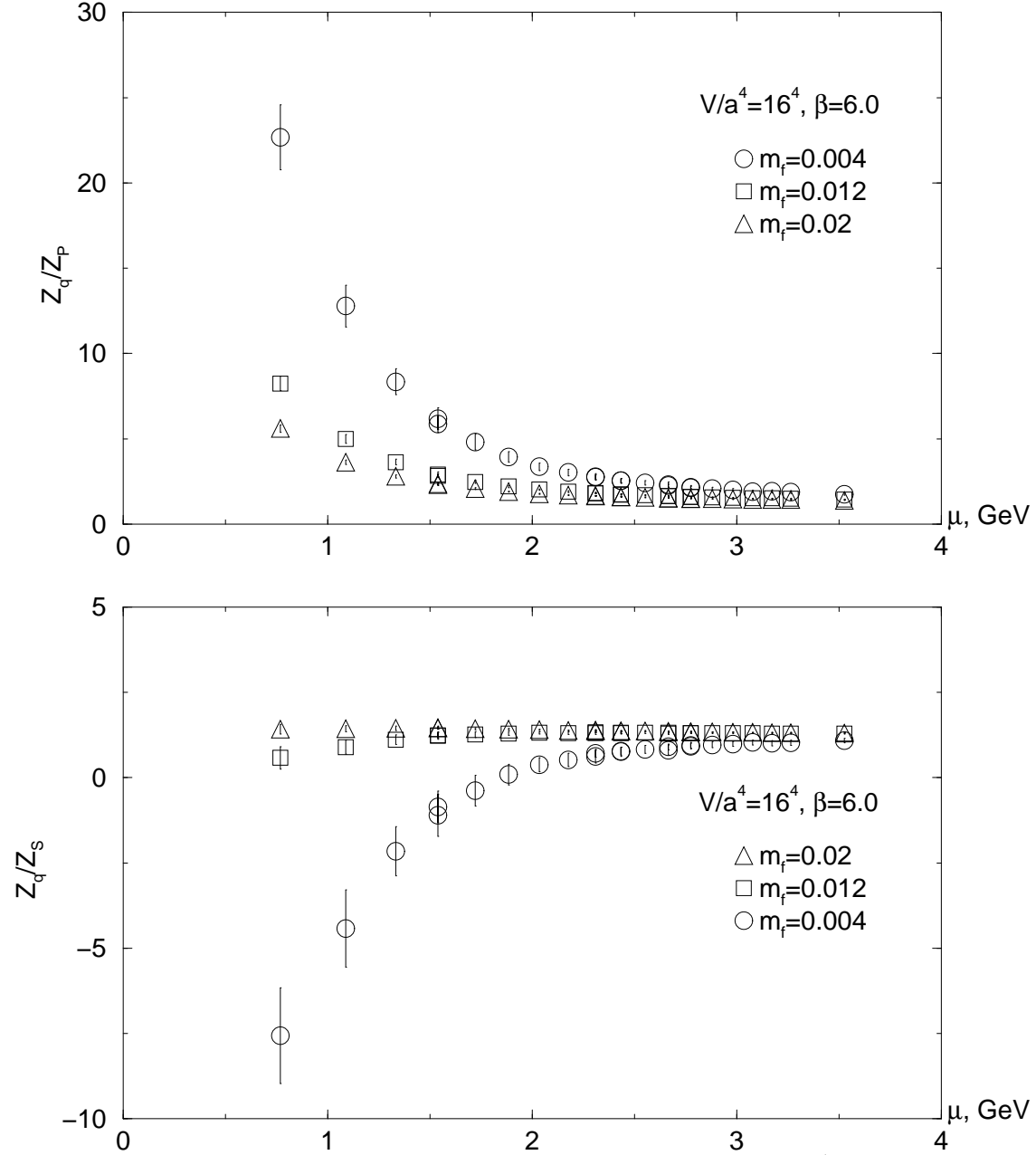


FIG. 5. Mass poles in the pseudoscalar and scalar operators in a 16^4 lattice volume at $\beta = 6.0$. These poles have to be subtracted at each momentum.

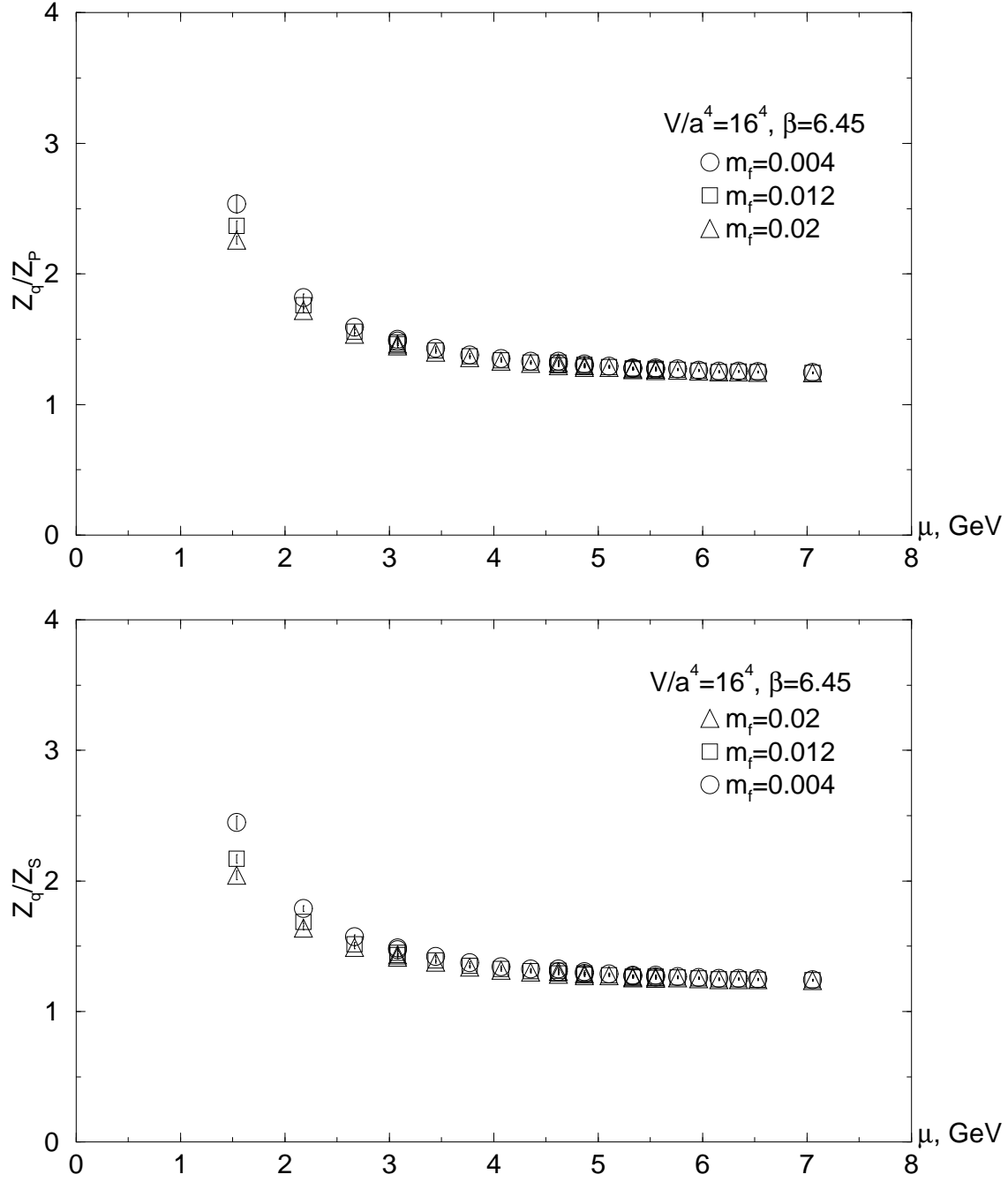


FIG. 6. Mass pole effects are much smaller at $\beta = 6.45$ in 16^4 lattice volume.

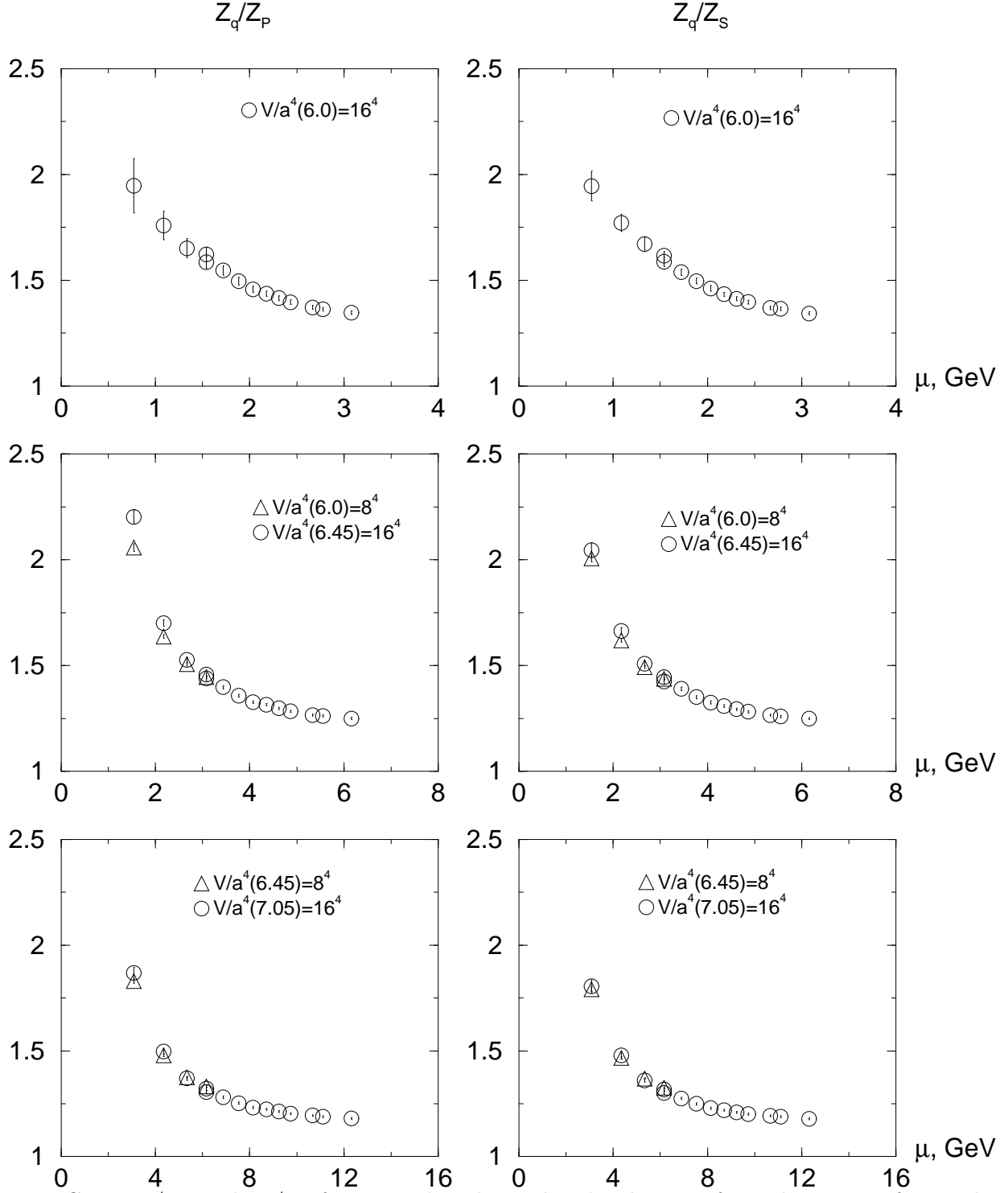


FIG. 7. Z_q/Z_P and Z_q/Z_S from pseudoscalar and scalar density after subtraction of m_f poles. The graphs from top to bottom correspond to different physical volumes, while each pair of graphs is for the same physical volume.

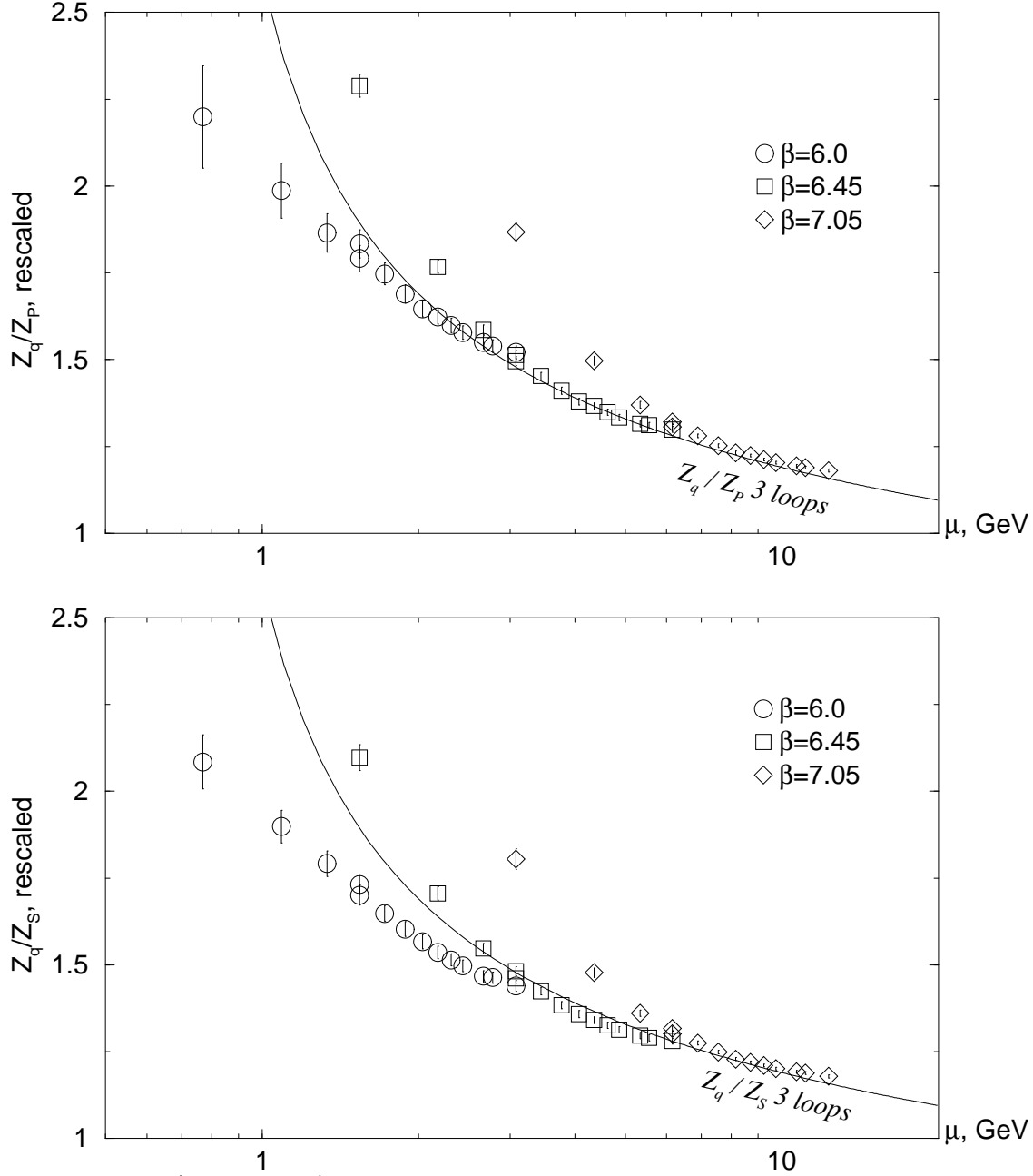


FIG. 8. Z_q/Z_P and Z_q/Z_S in a wide range of scales μ . All graphs have the same ultraviolet cutoff equal to the lattice spacing at $\beta = 7.05$. Different symbols correspond to different physical volumes (labeled by the β at which they are obtained). The finite volume effects are noticeable for momenta of the order of the inverse box size.

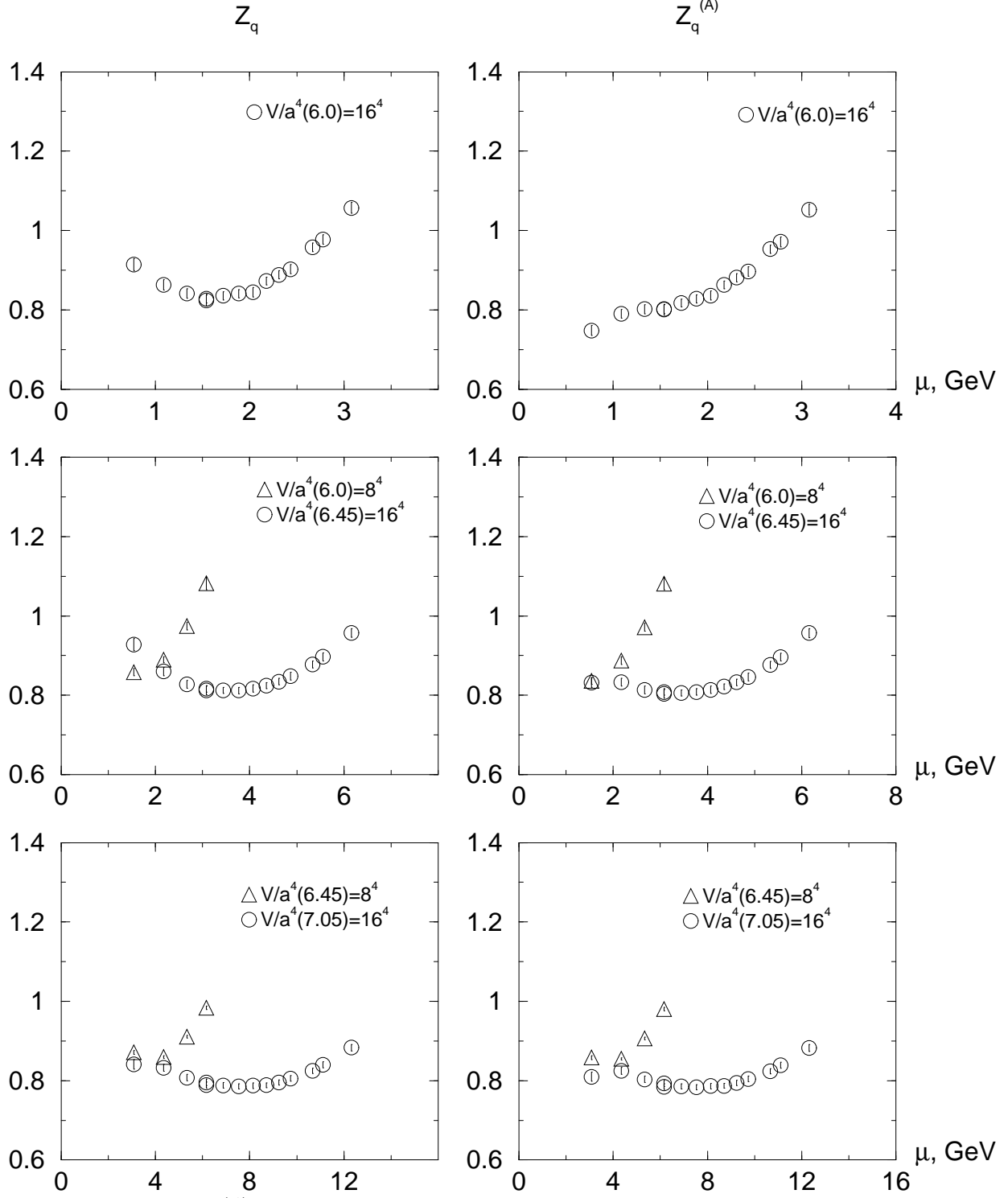


FIG. 9. Z_q and $Z_q^{(A)}$ from conserved vector and axial currents. The graphs from top to bottom correspond to different physical volumes, while each pair of graphs is for the same physical volume.

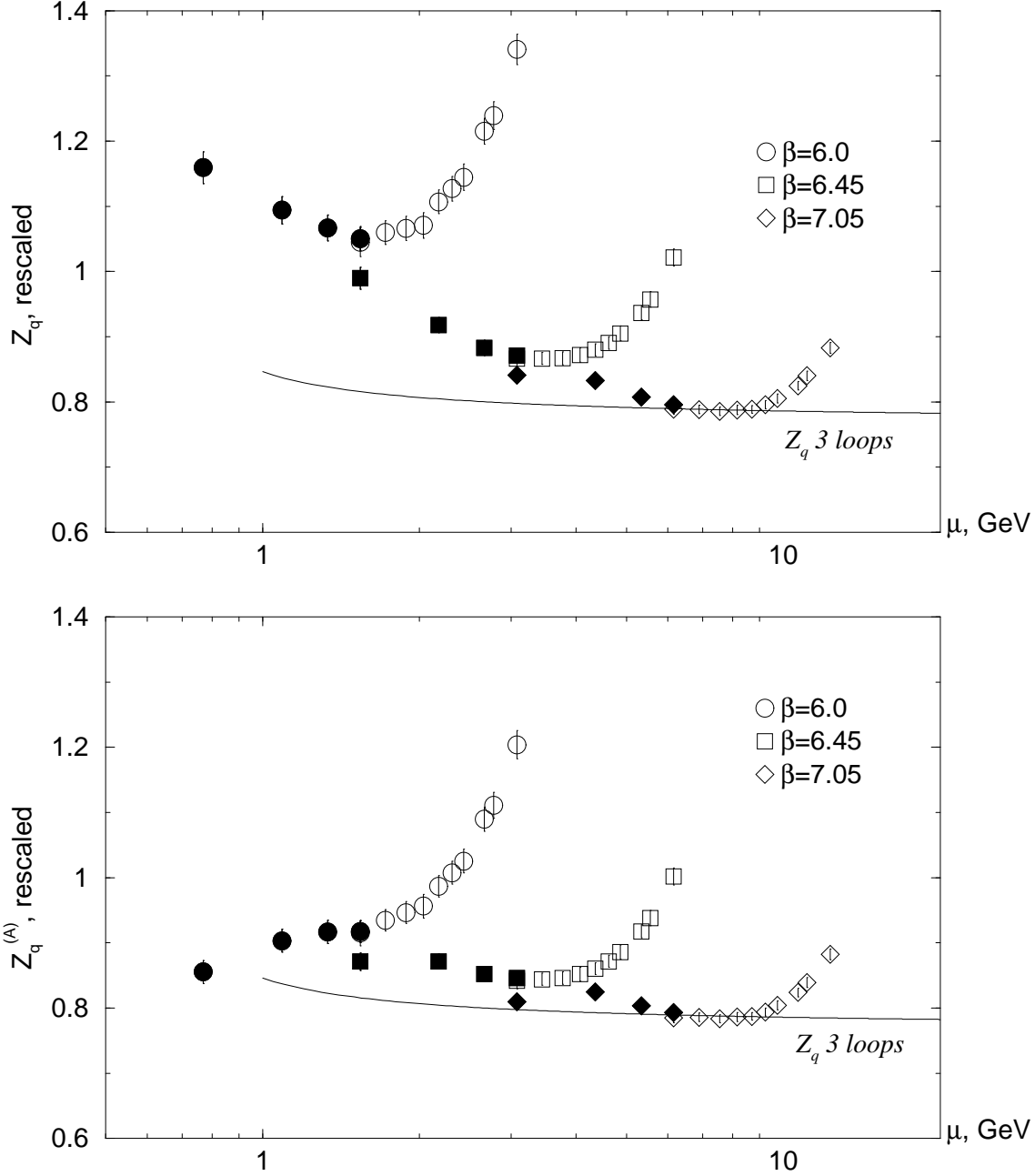


FIG. 10. Z_q and $Z_q^{(A)}$ plotted for a wide range of scales μ . All graphs have the same ultraviolet cutoff equal to the lattice spacing at $\beta = 7.05$. Different symbols correspond to data in different physical volumes (labeled by the β at which they are obtained). Solid symbols are for data with small discretization errors.

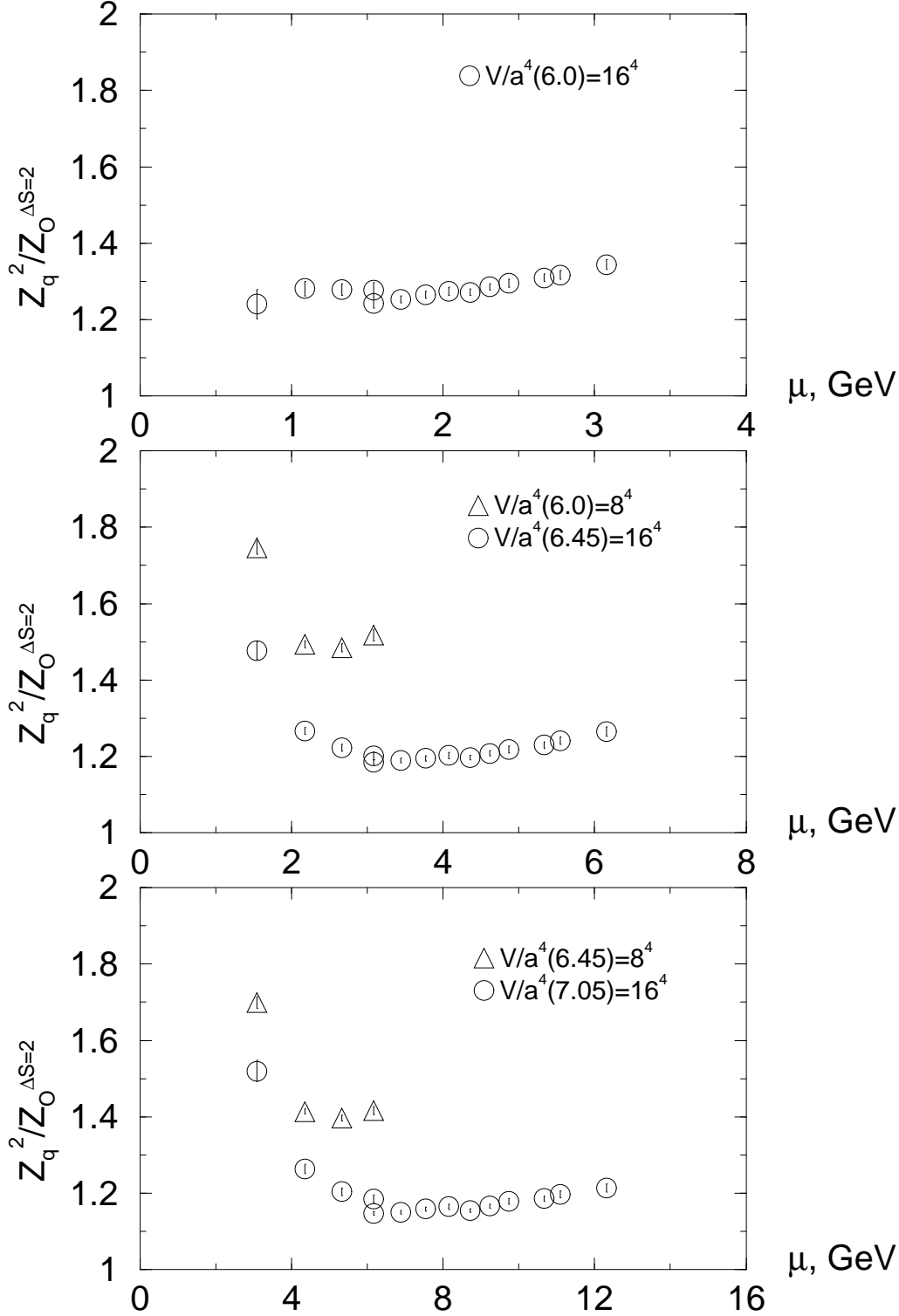


FIG. 11. $Z_q^2/Z_{O_{LL}^{\Delta S=2}}$ in the chiral limit from local vector and axial currents. The graphs from top to bottom correspond to different physical volumes, while each pair of graphs is for the same physical volume.

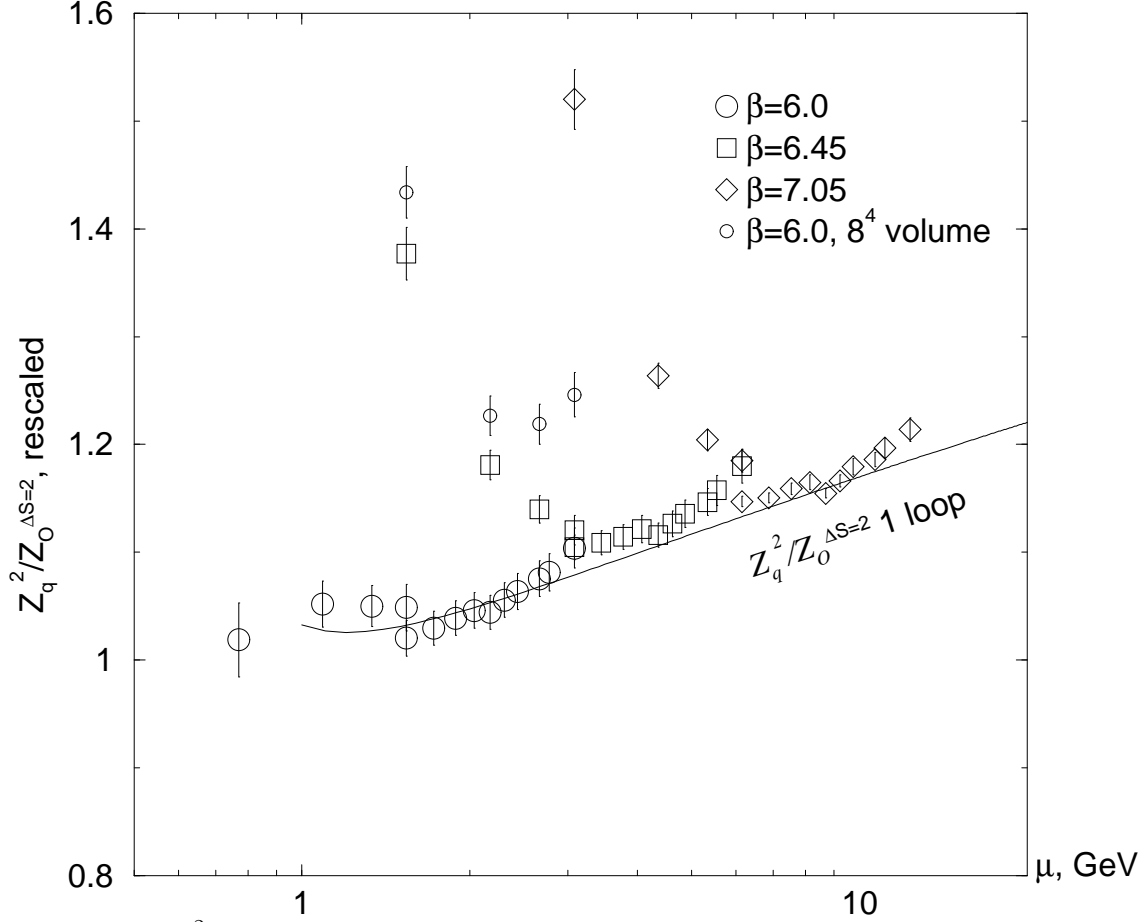


FIG. 12. $Z_q^2/Z_{O_{LL}^{\Delta S=2}}$ plotted for a wide range of scales μ . All graphs have the same ultraviolet cutoff equal to the lattice spacing at $\beta = 7.05$. Different symbols correspond to data in different physical volumes (labeled by the β at which they are obtained). The finite volume effects are large for momenta on the order of the inverse box size. Large symbols correspond to the 16^4 lattice volume. Small circles denote data obtained in a 8^4 volume at $\beta = 6.0$. Since no relative renormalization is involved for the two calculations at $\beta = 6.0$, the difference between the points is due to the finite volume effects only. The difference between the small circles and squares is due to discretization errors at the corresponding momenta. These errors are larger for the results obtained at the smaller $\beta = 6.0$.